The Effect of Strain Rate on the Tensile Deformation Behavior of Single Crystal, Ni-Based Superalloys

Y.M. WANG-KOH, O.M.D.M. MESSE, C.W.M. SCHWALBE, C.N. JONES, and C.M.F. RAE

Single crystal Nickel-based superalloys exhibit an anomalous yield point, the yield stress increasing with temperature to a maximum at around 750 °C. Here, we demonstrate in the alloy CMSX-4 at 750 °C that, although there is virtually no effect of strain rate on the initial yield point, at slow strain rates a second mechanism can initiate leading to a considerable softening effect. By examining the microstructures of a series of interrupted tests, this is attributed to the initiation of stacking fault shear after the operation of a secondary slip system. Using high-resolution TEM, the dislocation structures are shown to be identical in both structure and in the segregation of Co, Cr, and W, to those observed during creep deformation of single crystal alloys, although the conformation of the dislocations and faults differs from that observed during creep. This drop in flow stress at low strain rates is not observed in the alloys TMS138A and SRR99, in the former case, the improved creep resistance of this fourth-generation alloy would require a much slower strain rate to match the creep rate achievable at this temperature.

I. INTRODUCTION

HISTORICALLY, mechanical tests have been separated into creep, tensile, and fatigue. While from a macroscopic perspective, the deformation associated with each of these tests results in significantly different mechanical behavior and fracture surfaces, the dislocation–precipitate interactions which govern such macroscopic behavior are shared. In single crystal superalloys, these are dependent upon temperature, stress, strain rate, alloy chemistry, crystal orientation, and γ' precipitate size and morphology. At high stresses, above the yield point, shearing of γ' precipitates occurs *via* the coupled motion of paired $a/2\langle 110 \rangle$ dislocations, known as Anti-Phase Boundary (APB) shearing. Dislocations subject to cross-slip to the {001} plane lower the APB energy, a process that locks the dislocations known as Kear-Wilsdorf locking.[1–4] At high temperatures (> 850 °C) and low stresses, individual, unpaired $a/2\langle 110 \rangle$ dislocations are better able to bypass γ' precipitates by thermally activated climb.[5–7] In addition, other precipitate shearing mechanisms have been identified such as microtwinning[8] or formation of superlattice stacking faults.[9] Despite the number of studies on the specific deformation mechanisms, the transitions have seldom been investigated. It has been shown that strain rate can affect the deformation mechanism for tensile deformation. In a directionally solidified (DS) new Ni-Co superalloy, a drop in strain rate has been shown to induce shearing of the γ' precipitates by stacking faults (SFs).[10] This was attributed to the low stacking fault energy caused by high cobalt (> 20 pct). Smith *et al.* have shown that an increase in titanium, tantalum, and niobium content of a superalloy can control the transition between stacking fault shearing and microtwinning.[11] In addition, in polycrystalline Ni-based superalloys and steels, the decrease in strain rate is also accompanied by a transition from stacking fault formation to microtwinning.[8,12,13]

In this paper, the transition from tensile deformation to creep-like deformation as a function of strain rate is investigated. We show that creep deformation and tensile testing form a continuum, dislocations responding to the local conditions they experience.

Y.M. WANG-KOH and C.M.F RAE are with the Department of Materials Science and Metallurgy, University of Cambridge, 27 Charles Babbage Road, Cambridge, CB3 0FS, UK. Contact e-mail: cr18@cam.ac.uk O.M.D.M. MESSE is with the Oerlichen, Munich, Germany. C.W.M. SCHWALBE is with the Department of Materials Science and Metallurgy, University of Cambridge and also with the MTU Aero Engines AG, Munich, Germany. C.N. JONES is with the Rolls-Royce plc, PO Box 31, Derby DE24 8BJ, UK.
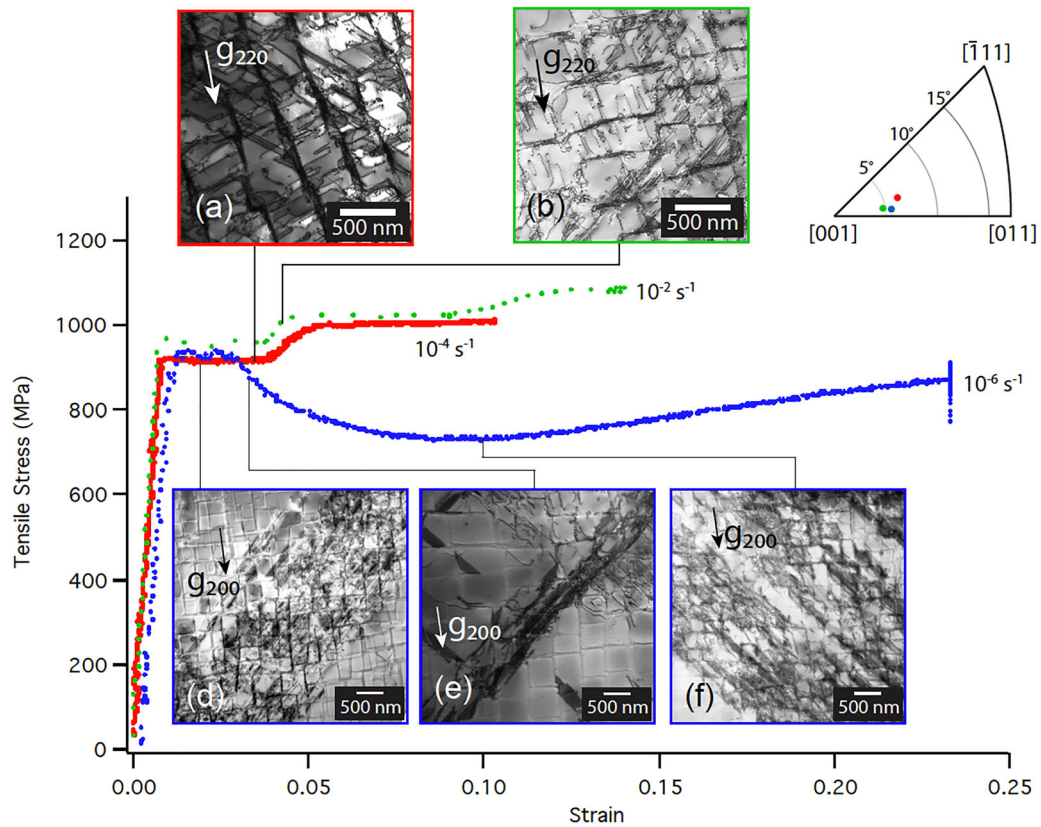
Fig. 1—Tensile stress–strain curves of CMSX-4 deformed at 750 °C at three different strain rates, $\dot{\varepsilon}$: 10^{-2} s^{-1} (green), 10^{-4} s^{-1} (red), and 10^{-6} s^{-1} (blue). Samples tested to failure. (a), (b), (d)–(f) TEM micrographs with two-beam contrast as indicated. These are shown at higher resolution in Fig. 2, and the Figure letters match with those of Fig. 2. There is no (c). (a) From a tensile specimen tested at a strain rate $\dot{\varepsilon} = 10^{-4}$ s^{-1}, interrupted at 3.3 pct strain. (b) From a tensile specimen tested at a strain rate $\dot{\varepsilon} = 10^{-2}$ s^{-1} interrupted at 4.8 pct strain. (d) to (f) From a tensile specimen tested at a strain rate $\dot{\varepsilon} = 10^{-6}$ s^{-1}. (d) Interrupted at 1.2 pct strain. (e) Interrupted at 2.7 pct strain. (f) Interrupted at 10.2 pct strain. The inset shows an inverse pole figure of the orientations of the three specimens tested to failure in relation to the [001] tensile direction (Color figure online).

II. EXPERIMENTAL

A. Alloys

CMSX-4, is a second-generation Ni-based single crystal superalloy, widely used in turbine blade applications. CMSX-4 was used for the principal matrix of experiments but was supplemented by work on two further superalloys, SRR99 and TMS-138A, to investigate how alloy composition influences the effect of strain rate on tensile deformation. SRR99 is a high diffusion first-generation superalloy and TMS-138A is a fourth-generation superalloy.[14] Compositions of the alloys in wt pct are given in Table I.

All superalloy materials were provided by Rolls-Royce plc., Derby, UK. Prior to machining, the specimens were homogenized, subjected to a heat treatment and aged: the primary age cycle was 2 h at 1140 °C and the secondary age was performed for 16 h at 870 °C. Microstructures of the specimens before testing were composed of cubic γ' precipitates measuring about 350 nm along their edges separated by γ-channels about 50 nm in width, containing small spherical tertiary γ' precipitates about 5 nm. The volume fraction of γ' was roughly 75 pct.

CMSX-4 exhibits a peak yield stress at 750 °C and this was therefore chosen as the benchmark temperature to conduct and compare these tensile tests. Three strain rates were chosen: 10^{-2} s^{-1}, 10^{-4} s^{-1}, and 10^{-6} s^{-1}.

B. Testing

Tensile specimens for these tests were machined from the commercial single crystal Ni-based superalloys CMSX-4, TMS-138A, and SRR99. Threaded tensile samples had a nominal gauge diameter of 3.5 mm and a gauge length of 25 mm. The specimen orientations were acquired using the SCORPIO system (Single Crystal Orientation Rapid Processing and Interpretation) at Rolls-Royce plc.[16,17] and are detailed in Table II. For all specimen tested, the angles (θ) between the [001] specimen axes and the loading direction were less than 10 deg to minimize the effect of orientation on results. High temperature, strain-controlled tensile tests were performed using an Instron 8501—100 kN servo-hydraulic machine. The tensile tests were performed at three different strain rates: $\dot{\varepsilon} = 10^{-2}$ s^{-1}, 10^{-4} s^{-1}, and 10^{-6} s^{-1}.

Alloy wt pct	Cr	Co	Mo	W	Al	Ti	Ta	Re	Ru	Hf	Ni
CMSX-4	6.5	9.6	0.6	6.4	5.6	1.0	6.5	3	—	0.1	base
TMS-138A	3.2	5.8	2.8	5.6	5.7	—	5.6	5.8	2.8	—	base
SRR99	8.5	5	—	9.5	5.5	2.2	2.8	—	—	—	base

Table II. Details of Tests Performed Including Strain Rate, Strain, and Orientation of the Specimen Where ρ Deg is the Deviation of the Tensile Axis from the [001] Direction and θ Deg the Rotation of the Plane Containing the Tensile Axis and [001] from the (100) Plane

Alloy	$\dot{\varepsilon}$ (s^{-1})	Strain at Interruption (Pct)	Strain at Failure (Pct)	Orientation (ρ deg/θ deg)	Comments
CMSX-4	10^{-2}	4.8		—	
	10^{-2}		14.9	4.8/8.8	green Fig. 1
	10^{-4}	3.4		6.9/31.3	after yield
	10^{-4}		10.7	7.7/12.2	red Fig. 1
	10^{-6}	1.2		5.8/24.2	at yield
	10^{-6}	2.7		6.9/31.3	after yield
	10^{-6}	10.2		5.4/21.7	stress drop
	10^{-6}		23.1	5.6/6.7	blue Fig. 1
TMS 138A	10^{-4}		10.8	6/1	
	10^{-6}		8.8	4.4/21.3	
	10^{-4}		12	4/22	
	10^{-6}		12.6	4/22	

1. TEM

To better visualize the dislocation structures associated with the deformation sustained during the mechanical tests, the primary slip plane and other crystallographic planes were determined. Back-Laue X-ray diffraction, using a Laue back-reflection camera with unfiltered Mo radiation, was employed to determine the orientation of the tensile specimen. This informed sectioning of the tensile specimen into transmission electron microscopy (TEM) foils along specific crystallographic planes. The TEM foils were prepared from 3 mm diameter spark-eroded discs with a thickness of ~150 μm and further electropolished using a Struers Tenupol-5 with a solution of 6 vol pct. perchloric acid in methanol, maintained at 20.5 V and -5 °C.

The TEM investigations were performed using a JEOL—200CX microscope, as well as a FEI Tecnai Osiris 80–200 equipped with an FEI Super-X EDX system employing four Bruker silicon drift detectors for high collection efficiency (> 0.9 Steradian) and high count rates (> 250 kcps). High-resolution TEM investigations were also conducted on an FEI Titan3 with a CEOS CESCOR hexapole aberration corrector in the probe forming lens. Complementary to the energy-dispersive X-ray spectroscopy (EDS) investigations carried out in the Tecnai Osiris, electron energy loss spectroscopy (EELS) maps were obtained from the FEI Titan microscope following TEM imaging to ascertain local chemical variation within the γ' precipitates where the faults were identified. The EELS maps were collected using a Gatan Tridiem 865 imaging filter, and the data were analyzed using Digital Micrograph software.

Although the HAADF imaging itself is capable of resolving the atomic columns in the thinner regions of the sample, the obtained digital images were subjected to a number of processing steps and numerical analysis in order to enhance and emphasize the observed features. The purpose of the analysis was to locate each column of atoms, quantify the degree of centro-symmetry for each, and thus identify faults in the stacking sequence. All the stages of the processing sequence were performed using MATLAB© with the Image Processing Toolbox. The center of symmetry analysis used in this study is based on the procedure outlined by Li.[15]

III. RESULTS

A. Tensile Stress–Strain Curves and Corresponding Microstructures

Figure 1 shows the stress–strain curves obtained from tensile tests on specimens of CMSX-4, tested to failure at 750 °C for three different strain rates, $\dot{\varepsilon}$: 10^{-2} s^{-1} (green curve), 10^{-4} s^{-1} (red curve), and 10^{-6} s^{-1} (blue curve). The orientations of each specimen are shown in the inverse pole figures with corresponding colors. All tests show a sharp yield at around 950 MPa. The plastic strain induced at this point is approximately 1 pct. Initially all tests strain without further increase in stress but then diverge. At the lowest strain rate, 10^{-2} s^{-1}, an abrupt rise in stress to 1000 MPa occurred at around 4 pct strain before plateauing again until 9 pct strain, at which point the stress increased gradually, failing at
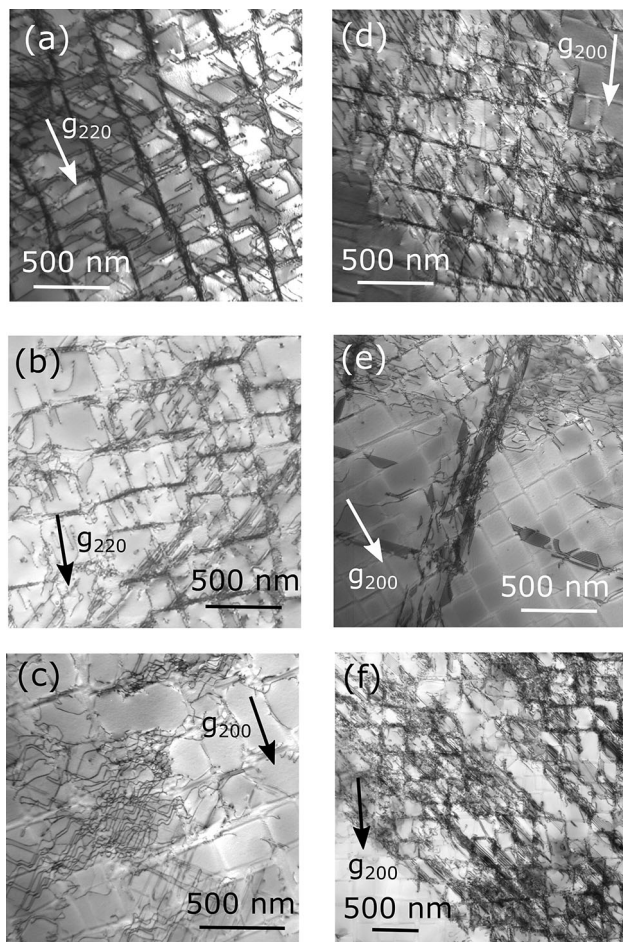
Fig. 2—TEM bright-field images of the microstructure from a CMSX-4 tensile specimens deformed at various strain rates and interrupted as follows: (a) tested at a strain rate $\dot{\varepsilon} = 10^{-4}$ s^{-1}; interrupted at 3.3 pct strain; (b) tested at a strain rate $\dot{\varepsilon} = 10^{-2}$ s^{-1} interrupted at 4.8 pct strain; (c) tested at a strain rate of 10^{-4} s^{-1}, interrupted before the yield point. (d) to (f) From a tensile specimen tested at a strain rate $\dot{\varepsilon} = 10^{-6}$ s^{-1}; (d) Interrupted at 1.2 pct strain; (e) Interrupted at 2.7 pct strain; (f) Interrupted at 10.2 pct strain.

around 15 pct strain. The test at 10^{-4} s^{-1} maps a similar path, but after increasing in stress at around 4 pct strain to 1000 MPa, shows no further increase before failure at a lower strain of 11.5 pct. The test at 10^{-6} s^{-1} exhibited the shortest plateau; the stress remaining at 950 MPa until around 3 pct strain before the stress drops gradually to 750 MPa at around 8 pct strain. After this, the stress rises more slowly before failing around 23 pct strain.

Further tests were run at the three different strain rates and interrupted at key stages in the deformation: after the yield point, after the second rise at 10^{-4} s^{-1}, and at the minimum stress at 10^{-6} s^{-1}. For the strain rate at 10^{-2} s^{-1}, a tensile test was interrupted at 3.4 pct strain. Another tensile test was run at 10^{-4} s^{-1} to 4.8 pct strain. Three further tests run at the strain rate 10^{-6} s^{-1} and were interrupted at strains of 1.2 pct, 2.7 pct, and 10.2 pct. The test-pieces were grouped into similar orientations to minimize the effect of orientation. Interruption strains were chosen to correspond to key

points. The interrupted stress strain curves overlap consistently with the tests run to failure. The interrupted test run to 10.2 pct strain at 10^{-6} s^{-1} was not recorded due to instrument failure.

TEM foils were produced from the interrupted test specimens of CMSX-4 by sectioning perpendicular to the tensile axis. A test interrupted prior to the yield point is shown in Figure 2(c). It is apparent that there is already considerable activity in the horizontal γ channels and in some of the wider vertical channels but not in the γ'. This limited plasticity explains why the strain at yield is about 1 pct.

Figure 2 shows enlarged TEM micrographs from the strategically interrupted specimens imaged close to the [001] zone axis, with two-beam bright-field conditions as indicated. Labels point to the appropriate interruption point on the tensile curves. Figure 2(a) shows a strain rate 10^{-4} s^{-1}, at 750 °C, interrupted shortly after yield at 3.3 pct strain. The sample shows discrete localized deformation bands and the image is taken from one of the localized deformation bands, and much of Figure 2(b), deformed at a higher strain rate 10^{-2} s^{-1} and to slightly higher strain of 4.8 pct, shows a very similar dislocation structure within the deformation bands. Figure 2(c) is tested at a strain rate 10^{-4} s^{-1}, at 750 °C, and interrupted shortly before yield. It shows substantial dislocation activity confined to the γ' phase prior to yield, consistent with the high strains indicated prior to the yield point.

The TEM micrographs for interrupted specimens at the slowest strain rate, 10^{-6} s^{-1} are shown in Figures 2((d) through (f)). Interrupted at 1.2 strain (Figure 2(d)), the tensile specimen has reached a stress plateau and, as at the faster strain rates, dislocations are confined to distinct slip bands with some areas of the microstructure free of any dislocations. However, at 2.7 pct strain (Figure 2(e)), stacking faults appear in the slip bands on multiple planes. Portions of the microstructure remain free from dislocations. The stress continues to drop and the TEM micrograph, interrupted at 10.2 pct, at the minimum stress, (Figure 2(f)) shows these slip bands have widened to cover much of the microstructure.

A further image from CMSX-4 deformed at 10^{-2} s^{-1} and sectioned perpendicular to the tensile axis (similar to Figure 2(b)) is shown in Figure 3. In addition to the dislocations in the γ phase, there are also dislocation visible as pairs, dipole pairs and paired loops in the γ'. The dislocations in the γ' precipitates are all APB pairs cross-slipped onto the vertical cube plane and hence appear as single dislocations from this viewpoint.

Tensile tests were also run for two further alloys: TMS-138A and SRR99, across two strain rates: 10^{-4} s^{-1} and 10^{-6} s^{-1}. The tensile curves to failure are shown in Figure 4. The respective orientations for each tensile specimen are shown on the inverse pole figure inset of Figures 1 and 3. The yield stress of the fourth-generation alloy TMS-138A has a noticeably lower yield stress at 860 MPa than CMSX-4 at about 940 MPa. The first-generation alloy SRR99 yields at the highest stress of 1020 MPa. Both alloys follow the same trend of plateau in the flow stress followed by an abrupt rise in
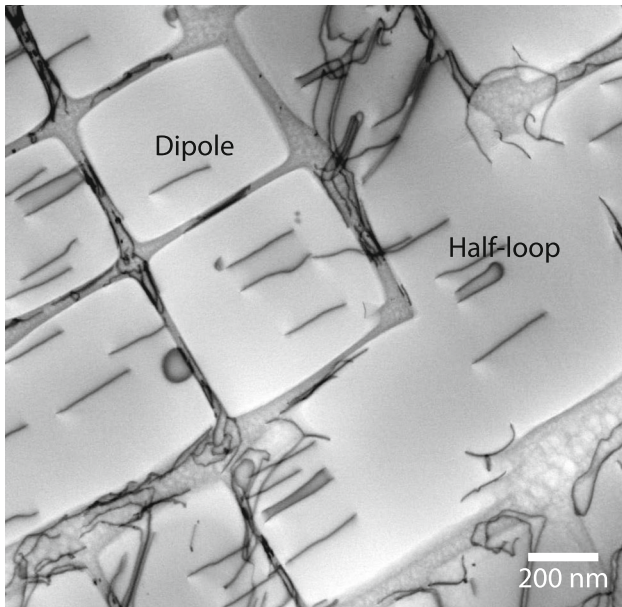
Fig. 3—A STEM micrograph of the microstructure from a CMSX-4 tensile specimen, deformed at a strain rate of 10^{-4} s^{-1}, interrupted at 1.8 pct strain, cut and viewed down the [001] zone axis. Areas of darker contrast between dislocation pairs indicate dipoles and half-loops have been highlighted.

Fig. 4—Tensile stress–strain curves for (a) TMS-138A and (b) SRR99, all tested at 750 °C to failure at two strain rates: 10^{-4} s^{-1} (black curve) and 10^{-6} s^{-1} (red curve). Inset: inverse pole figures showing the orientations of the respective specimens in relation to the [001] tensile direction (Color figure online).

stress at about 3 pct strain. Testing at the slower strain rate of 10^{-6} s^{-1} gives a very similar curve in both cases with a slightly delayed rise in work hardening for TMS 138A and lower work hardening in both cases.

B. Further Analysis of Stacking Faults

To further investigate the stacking faults observed in Figures 1(d) and (e), the Laue back-reflection method was used to determine the primary slip system of the tensile specimens. This allowed for precise sectioning of the specimen; first parallel, then perpendicular, to the slip system on which the stacking faults were present. Conventional TEM imaging was performed on specimens cut parallel to the primary slip system, exposing the stacking faults within the plane and dislocations that bound such faults.

Figure 5 shows the microstructure of the tensile specimen deformed at a strain rate of 10^{-6} s^{-1} to 2.7 pct strain, cut on the $(1\bar{1}1)$ plane, the primary active slip plane. In the middle, Figure 5(a) shows a schematic illustration of the dislocation structure. It shows a stacking fault spread on the $(1\bar{1}1)$plane, bounded by a total of six dislocation lines, four on one edge, two on the other, shearing a γ' precipitate. The dislocations cross both γ' precipitates and the γ-channels and from their shape seem to progress more easily in the channels than the precipitates. To determine the Burgers vectors of the dislocations forming this faulted structure, a Burger's vector analysis was conducted, comparing the six different two-beam conditions around the $[1\bar{1}1]$ zone axis. The surrounding six images are STEM micrographs taken under six different two-beam conditions, at
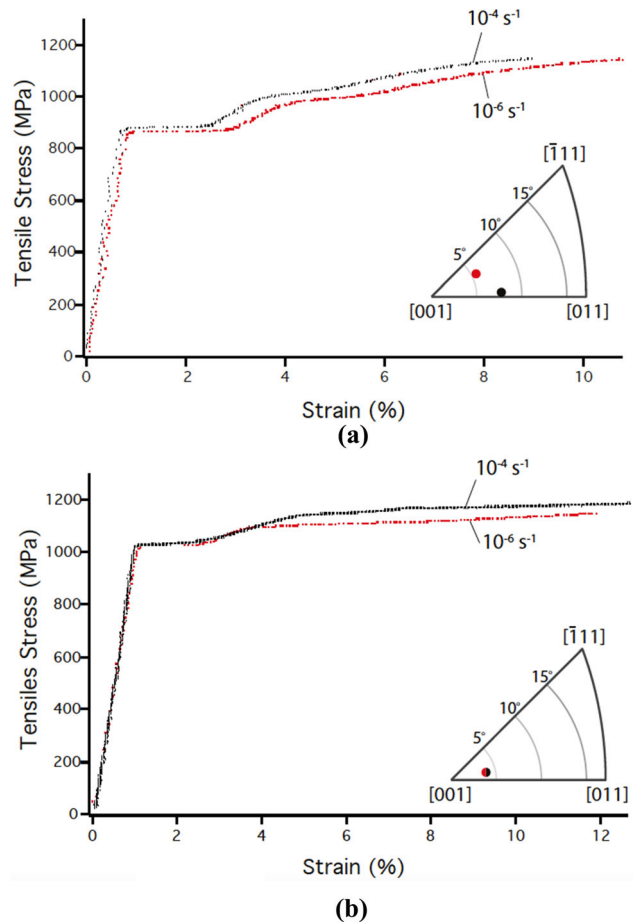
different degrees of rotation away from the $[1\bar{1}1]$ zone axis. The white arrows indicate the g-vectors, pointing in the direction of the respective reciprocal lattice planes highlighted by the red planes in the subfigure. Dislocations having Burger's vectors lying in the diffraction plane would appear invisible in the STEM micrograph under that two-beam imaging condition ($\mathbf{g.b} = 0$). By tilting the sample to the six different two-beam conditions of Figure 5, the Burgers vectors of the dislocations that bound the stacking fault can be deduced.

The six dislocations, labeled 1–6 in Figure 5, are graded on a 3-point scale of visibility: i invisible, w weak, visible but not prominent and v visible in Table III. From this it can be concluded that the dislocations all have a Burger's vector in the direction [121]. This is demonstrated by the $g = (\bar{2}02)$ imaging condition, where none of the dislocations are visible. The six individual dislocations are most clearly distinct as they pass through the γ phase in the area at the center of the micrographs; in other cases, they are too closely spaced to establish whether they are superpartials or dissociated partials.
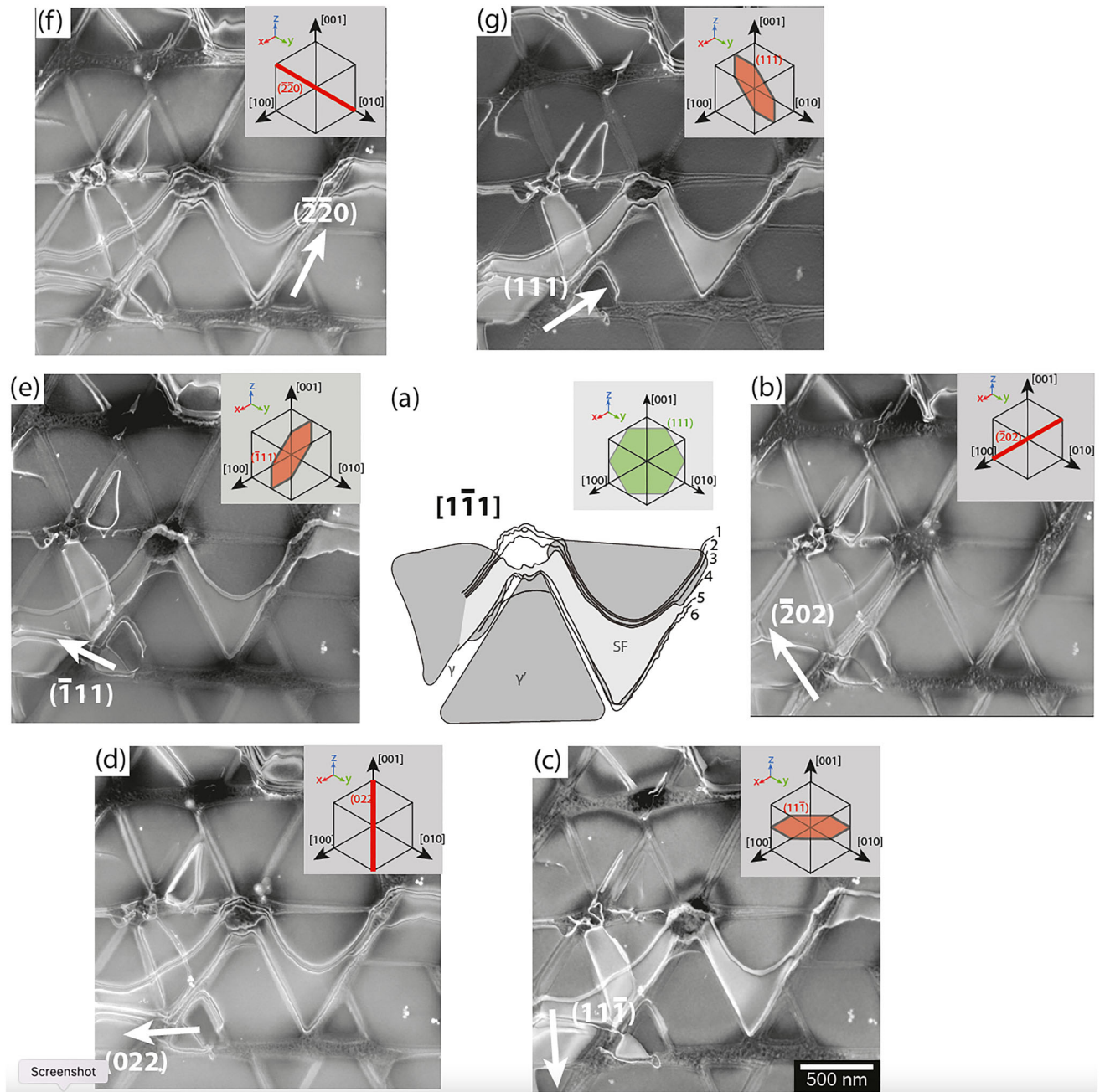
Fig. 5—STEM micrographs of the microstructure from a CMSX-4 tensile specimen deformed at a strain rate of 10^{-6} s^{-1} to 2.7 pct strain, at 750 °C, cut on the (1$\bar{1}$1)plane. All sub figures are taken over the same area of the sample. Starting at the center and then right, going clockwise: (*a*) A schematic illustration of the dislocation structure, down the [1$\bar{1}$1] zone axis. (*b*) Two-beam contrast, *g* = ($\bar{2}$02). (*c*) *g* = (11$\bar{1}$). (*d*) *g* = (022). (*e*) *g* = ($\bar{1}$11). (*f*) *g* = ($\bar{2}\bar{2}$0). (*g*) *g* = (111). Highlighted planes which are parallel to the electron beam are shown in inset of each subfigure.

To understand further the atomic structure of these dislocations and stacking faults, the tensile sample was cut on the (011) plane, perpendicular to the slip plane, so that the Burgers vectors of the dislocations bounding either side of a shearing stacking fault would have its maximum edge component perpendicular to the cut plane. Cutting on this plane can also establish the magnitude of the Burgers vectors of the dislocations.

Figure 6 shows a HAADF-STEM image of a stacking fault captured edge-on, down the [$\bar{1}$01] zone axis. A fault can be seen propagating from right to left with the leading dislocation highlighted in the HAADF condition. Tertiary γ' precipitates in the γ-channel are also visible. Lattice imaging of the leading dislocation structure is presented in Figure 6(a). The end of the stacking fault has a higher contrast to the background.

To locate the SF precisely, a Center of Symmetry analysis was performed on the processed image (Figure 7(a)) identifying those atom locations which are not symmetric and hence do not have regular fcc

g	[$\bar{1}$11]	[11$\bar{1}$]	[111]	[$\bar{2}\bar{2}$0]	[022]	[$\bar{2}$02]	Burger's Vector
1	w*	v	v	v	v	i	[121]
2	v	v	w	v	v	i	[121]
3	i/w*	i/w*	v	v	v	i	[121]
4	i/w*	i/w*	w	v	v	i	[121]
5	v	v	v	v	v	i	[121]
6	v	v	v	v	v	i	[121]

Dislocations in **g**-conditions labeled'*' are not clear due to dislocation interactions and strain contrast. [*i* invisible, *w* weak, *v* visible].

Fig. 6—A HAADF-STEM micrograph of a stacking fault imaged down the [$\bar{1}$01] zone axis from a tensile specimen of CMSX-4, deformed at 750 °C at a strain rate of 10^{-6} s^{-1} interrupt at 2.7 pct strain. A stacking fault can be seen propagating from right to left, with the leading dislocations highlighted.

stacking, Figure 7(b). In this analysis, a single-layered Intrinsic SF appears as two adjacent rows without a center of symmetry, and an Extrinsic SF appears as two layers separated by a symmetrical layer, Figure 7(c) shows this enlarged. The imaged stacking fault is propagating from right to left. It shows a single-layered, "Superlattice Intrinsic Stacking Fault" (SISF) terminating as a two-layered, "Constricted Extrinsic Stacking Fault" (CESF-2), all within the γ' precipitate. The Burger's circuit traced around the entire fault segment passing through the SISF has a displacement vector of $b = a/3[121]$ in the observed plane. If measured with the circuit passing through the extrinsic end of the fault is half this value at $a/6[121]$ or 2/3 of the spacing of the center of symmetry points. This is consistent with a dissociated pair of partials in the γ' each having a Burger's vector of $a/6[121]$. The Burger's vector of the partial dislocations lies in the plane of the sample. Sectioning on the $\langle 011 \rangle$ plane perpendicular to the tensile axis and the primary slip plane will position the $\langle 121 \rangle$ with the highest resolved shear stress in the plane of the specimen, and hence it is not surprising that this is the active stacking fault shear system. This is indexed to be consistent with Figure 5 from the same test. The configuration observed shows the leading $a/3[121]$ superpartial dissociated into two identical $a/6[121]$ Shockley partials separated by a Complex Extrinsic Stacking Fault lying on adjacent planes. Counting the number of atoms rows at the bottom of the fault, the distance separating these two Shockley partials is approximately 13 lattice spacings or ~ 2.85 nm where the point spacing in the slip plane is $a/4[121]$.

Figure 8(a) shows a different stacking fault in the same area propagating from right to left. The leading edge of the faulted structure, labeled region 'A,' and a portion of the trailing fault labeled region 'B' all lie within the γ' precipitate. EDX maps were collected over regions A and B, in an interval of 2.5 nm with drift correction in place, to check for evidence of chemical variation at and around the stacking faults. The corresponding STEM-HAADF micrographs of regions A and B are shown in Figures 8(b) and (h), respectively. The compositional EDX maps for region A for the elements Cr, Co, Al, W, and Ni are shown in Figures 8((c) through (g)). The EDX maps for region B are shown in Figures 8((i) through (m)). Figures 8(c)
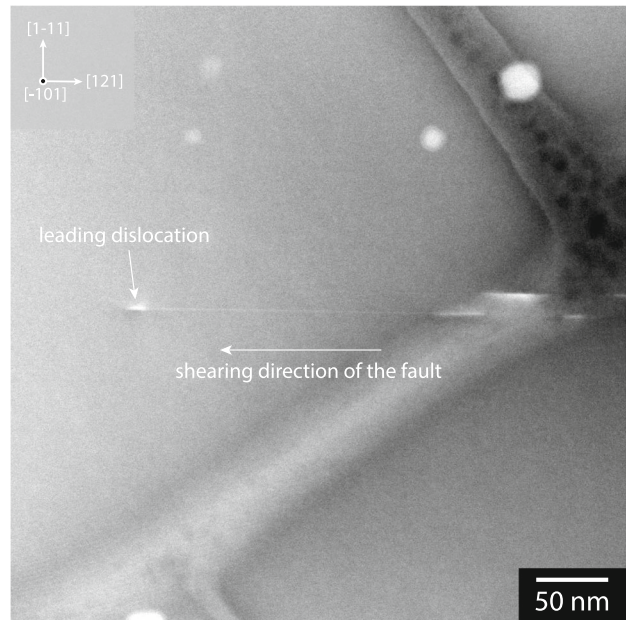
and (d) show segregation of chromium and cobalt, segregation is stronger at the front-end of the fault, section A. Al and Ni are depleted directly below the fault (Figures 8(d) and (f)), and Figure 8(e) shows a very slight enrichment of W in region A but this is not clear in Region B, Segregation of Co and Cr is observed evenly along the length of the fault in region B (Figures 8(i) and (j)), together with a depletion of Al (Figure 8(k)), despite the HAADF image showing non-uniform brightness across the length of the fault. To evaluate the relative enhancement of elements at the fault, EDX line scans were taken through the fault region. These are shown in Figure 9. It shows chromium and cobalt are enriched by around 2 at pct.

EELS mapping was also conducted in a region containing the middle part of a stacking fault and the adjacent area. Compositional maps were taken corresponding to the Cr L$_{2,3}$, Co L$_{2,3}$, and Ni L$_{2,3}$ edges and are shown with the STEM-HAADF survey image in Figure 10. An enrichment of chromium and cobalt and a depletion of Ni along the fault are just about visible, though the segregation to the fault is not as pronounced as in the EDX images. The images nevertheless support the EDX maps of Figure 8, that segregation of chromium and cobalt occurs to the stacking fault in this sample.

IV. DISCUSSION

A. Features of the Stress–Strain Curves

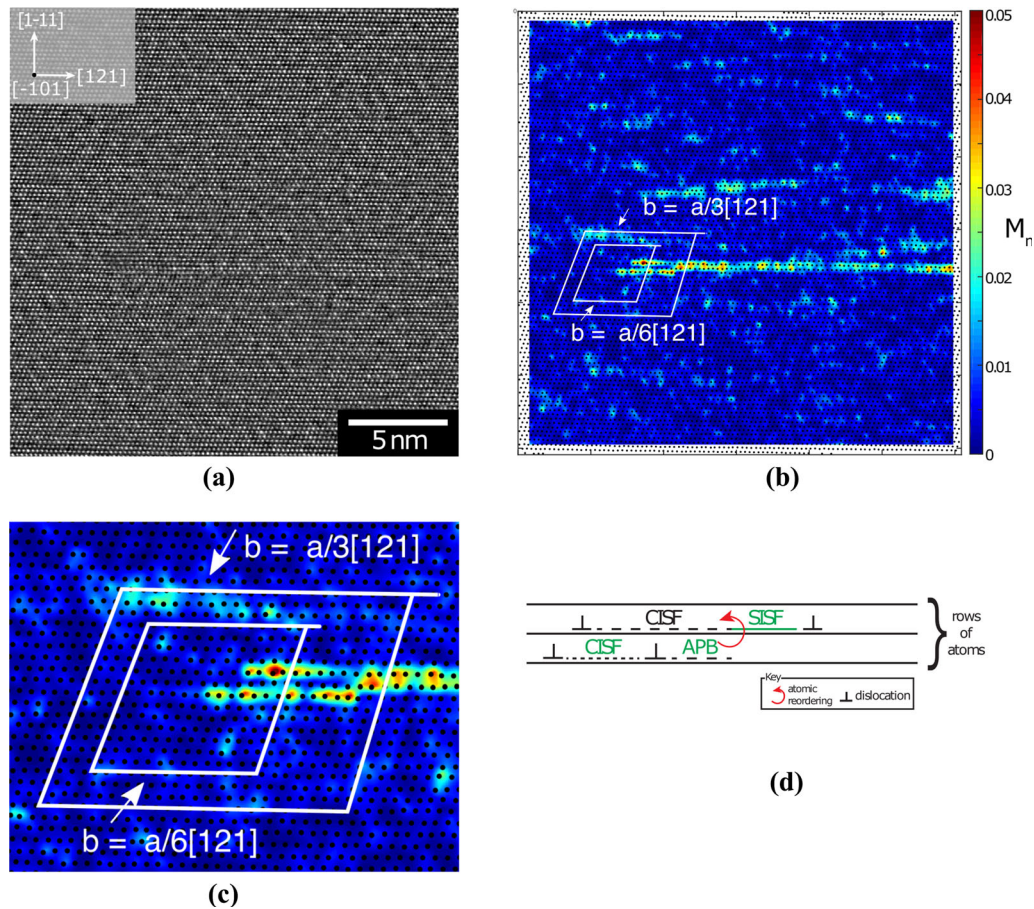Figure 4 shows the pre-yield behavior and the yield point vary, depending on the alloy. TMS-138A has a

Fig. 7—(*a*) A low-magnification HRSTEM image of a stacking fault from a tensile sample of CMSX-4 tested at 750 °C at a strain rate $\dot\varepsilon = 10^{-6}$ s^{-1}, interrupted at 2.7 pct strain. The sample has been cut on the (011) plane. The stacking fault is viewed edge-on and can be seen in both the γ' precipitate and γ channel. (*b*) The corresponding Center of Symmetry (CoS) mapping with Burgers circuit shows a fault which is spread over two layers. (*c*) An enlargement of the end of the Stacking Fault in (c). (*d*) A schematic illustration of the hypothesized mechanism for the formation of the leading edge of the stacking fault. A CESF-2 converts into a lower energy SISF by a reordering process.

yield point stress of 875 MPa, slightly lower than CMSX-4 at 920 to 940 Mpa. The first-generation alloys, SRR99, had the highest yield stress of 1030 MPa. However, the yield point is almost independent of strain rate for each alloy. There is potentially a small effect of orientation as the two curves for CMSX-4 and 138A, which result from the least well-matched of the samples, differing by about 20 MPa. The samples for SRR99 have similar orientations and show the same yield stress. The effect of orientation was not studied further in this work as the aim was to match the samples as much as possible. The APB energy has the major effect on yield stress,[18] but the lattice misfit between the γ and γ' phases may also affect the yield point as it changes the stress in the γ channels of the coherent microstructure, raising the effective shear stress in the horizontal channels and reducing it in the two vertical channels.[19,20]

The stress strain curves from specimens tested at strain rates of 10^{-2} s^{-1} to 10^{-6} s^{-1} show linear deformation up to a yield point around 950 MPa. At the yield point, the strain is ~ 1 pct, much higher than would result from elastic deformation alone and this is explained by the activity confined to the γ channels in

the sample interrupted before yield, Figure 2. The flow stress corresponds to the stress needed for dislocations to enter the precipitates. At yield, the interfacial dislocations, pinned up against the γ/γ' interfaces, experience a high enough stress to penetrate the γ' precipitates.

At the yield point, the dislocations are able to penetrate the γ' as pairs, overcoming the stress on the leading dislocation due to the APB fault created on entry. The initial yield results in narrow slip bands but, as the deformation proceeds, the slip bands increase in width. Some dislocation pairs cross-slip in the γ' onto the {100} plane, parallel to the tensile axis, and containing the Burger's vector of the dislocation pair.[2] These Kear-Wilsdorf locked dislocations are visible as dipole pairs and several examples can be seen indicated by white arrows in Figure 2(b). They are present in all the alloys after yield and were noted by Feller-Kneipmeier *et al.*[21,22] The dipole is believed to be formed when a moving pair cross-slips becoming immobile and hence causing the remaining section moving in that γ' precipitate to cross-slip as it rotates into the screw configuration parallel to the first section and, being immobilized by that, is more likely itself to also become
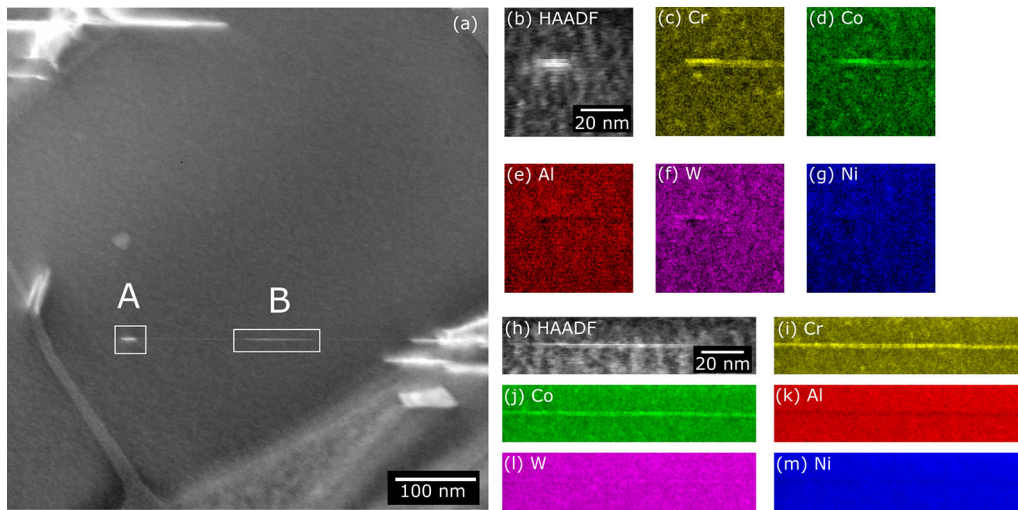
Fig. 8—EDX maps showing spatial distributions of the elements Cr, Co, Al, W, and Ni, taken over two regions of the microstructure from a sample of CMSX-4 deformed at a strain rate of 10^{-6} s^{-1} at 750 °C, interrupted at 2.7 pct strain. (*a*) A STEM-HAADF micrograph imaged down the [110] zone axis, showing a stacking fault in a γ' precipitate. The EDX scans were taken from the front of the fault and a section midway along the fault, labeled as scan regions 'A' and 'B,' respectively. (*b*) A HAADF image of the zoomed-in region 'A,' (*c*) to (*g*) shows the elemental EDX maps from region A for the elements Cr, Co, Al, W, and Ni, respectively. (*h*) shows a HAADF image of the zoomed-in region 'B,' (*i*) to (*m*) show the elemental EDX maps for region B for elements Cr, Co, Al, W, and Ni, respectively.

locked. These configurations and their evolution will be the subject of a later paper. Suffice to say, the presence of these locked dipole pairs prevents further deformation on the precise slip band and causes it to widen as strain increases. This is the case in Figure 1(e) where the slip bands have widened to cover most of the sample and there is relatively little dislocation-free microstructure. The availability of dislocation-free areas into which the slip bands can expand explains why deformation proceeds after yield for some considerable strain without an increase in the flow stress. Dislocations impinging on the locked dislocation pairs are able to climb to a parallel slip plane and continue at the same stress. This can occur in the γ or at the γ/γ' interface. The origin of the periodic step increases in stress with strain observed in all three alloys is currently under investigation. Progress of the dislocation pairs through the γ' appears to be rapid as dislocations are rarely seen traversing the precipitates in the interrupted tests except where they become locked in the screw orientations. Those investigated are invariably dissociated on the cube plane.

B. Stacking Fault Shear

During creep at temperatures around 750 °C and stresses below that necessary to allow dislocations coupled by APB faults enter the precipitates, deformation involves the cutting of the γ' precipitates by dislocations trailing stacking faults. There is a stress threshold for significant stacking fault shear in CMSX-4 of around 550 MPa with the strain rate increasing very rapidly with stress by a power law relationship.[10] In the case of ordered precipitates, the Burger's vector necessary to produce the low energy SISF has the Burgers vector $a/3 \langle 121 \rangle$. The faults are formed by the interaction of dislocations on two, separate slip systems with Burger's vectors at 60 deg to each other, to produce a

Stacking fault ribbon combining partial dislocations separated by SISF, SESF, and APB faults,[24,25]:

$$2 \times (a/2[011] + a/2[110]) \rightarrow a/6[121] + \text{CESF - 2}$$
$$+ a/6[121] + \text{SISF} + a/6[121] + \text{APB} + a/6[121]$$
$$+ \text{SESF} + a/6[121] + \text{CISF} + a/6[121]$$

$$[1]$$

where CISF is a complex intrinsic stacking fault and CESF-2 can be treated as an CISF over an CISF on two adjacent {111} planes (Figure 6(c)).

Figure 8 shows the leading edge of the fault featured in Figure 6 consists of a SISF in a γ' precipitate, terminating in a two-layer CESF-2-type fault. The dissociation of the Shockley partials bounding this complex stacking fault is so small that it is not conclusive in the dislocation analysis of Figure 5 in Table III, but it is clearly shown to be of the order of 3 nm in the HAADF images of Figure 7. This fault structure is identical to that previously observed in samples deformed under primary creep at intermediate temperatures (750 °C), including the separation of two partials (1 and 2 in Figure 4(a)) in the dislocations leading the fault.[23,24] The lower energy SISF fault forms from the CESF-2 by a reordering occurring at the second, trailing partial $a/6$ [121]. Kear *et al.* suggested such displacements can be achieved through atomic shuffles at the partial dislocations bounding the extrinsic fault,[25–27] and Kovaric *et al.* looked in detail at the atom movements likely in such a shuffle and the activation energies involved.[28] As in creep, the movement of these stacking fault ribbons requires atomic shuffles at the leading and trailing edges to proceed as illustrated in Figure 7(d).
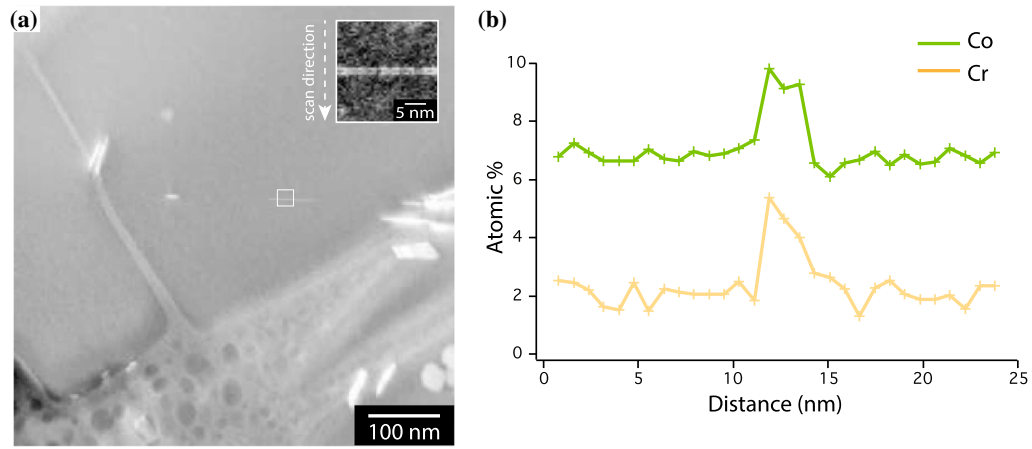
Fig. 9—EDX line scan of a stacking fault in CMSX-4. (*a*) A HAADF-STEM image viewed down the $[\bar{1}01]$ zone axis shows the position of the line scan relative to the fault and (*b*) EDX plots show concentration of chromium and cobalt at the fault.
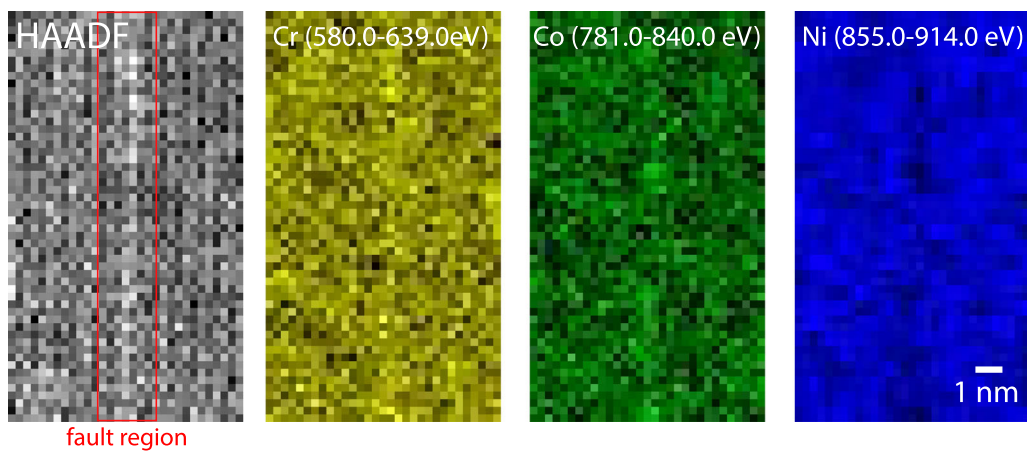

Fig. 10—STEM-EELS mapping of composition in the vicinity of a stacking fault. (*a*) STEM-HAADF survey image of the stacking fault and adjacent area used for EELS mapping. (*b*) to (*d*) Compositional maps corresponding to Cr $L_{2,3}$, Co $L_{2,3}$, and Ni $L_{2,3}$ edges, respectively.

The EDX maps in Figure 8 show enrichment of Cr and Co and, to a lesser extent, W at the leading edge of the fault. The enrichment of these elements implies that they lower the stacking fault energy,[29] hence segregation may be a necessary precursor to the formation of SISFs and SESFs. There is an enhanced segregation environment at the front of the fault (region A) compared to along its length (region B), characterized by higher Co and Cr levels and potentially enrichment of W Figure 8(f) which is not detectable in region B. Viswanathan *et al.*[30] showed a similar compositional variation exists at SISFs created in the γ' precipitates during creep in CMSX-4. Thus, the rate at which they move is fundamentally limited by the diffusion coefficients under the conditions of deformation, both self-diffusion for the shuffle, and the diffusion of segregants Co, Cr, and W to the fault. For this lower stress mechanism to operate, there must also be the appropriate combination of primary dislocations to produce the stacking fault ribbon, but also sufficient density of stacking fault ribbons to maintain the strain rate imposed by a tensile test. Nevertheless, because of the very large Burger's vector, a $\langle 121 \rangle$, it is a highly effective deformation mechanism where the conditions for it to operate are in place.

Initially, where only one slip system operates at yield, there is no capacity to produce stacking faults and APB shear is the only mechanism to operate producing a remarkably consistent yield point independent of strain rate. When sufficient dislocation density on a suitable secondary slip system develops, dislocations can combine with those of the primary slip system to produce stacking fault ribbons. Once formed, there are two competing deformation mechanisms for shearing precipitates: APB shearing and stacking fault shear. The stacking fault shear mechanism takes less stress compared to APB shearing but requires diffusion to activate and so, at low temperature, APB shearing is the default deformation mechanism. At a higher temperature or slower strain rate, stacking faults are observed in the γ' precipitates, as shown in Figures 1(d) and (e). The strain rate is related to the dislocation density by the Orowan Equation, Eq. [2], where ρ is the dislocation density, b is the Burgers vector of the dislocations, and v is the

average velocity of the dislocations and the subscripts depict the two mechanisms.

$$\dot{\varepsilon} = \rho_{APB}b_{APB}v_{APB} + \rho_{SF}b_{SF}v_{SF} \qquad [2]$$

At the slowest strain rate: $\dot{\varepsilon} = 10^{-6}\ s^{-1}$ (the blue curve in Figure 1), during the initial rising region of the curve, the material is being elastically loaded, but also experiencing some limited dislocation movement in the γ channels. At yield, the stress is high enough for these dislocations, pinned against the γ/γ' interface, to enter γ' precipitates. At this stage, deformation proceeds by APB shearing. Upon further deformation, a second slip system becomes active, as shown by two bands of dislocations in Figure 1(d), and these slip bands are on different slip planes as they intercept the sample perpendicular to each other. The interaction of dislocations in these two slip systems facilitates the formation of stacking faults and stacking fault shearing begins to occur. As strain increases, a greater proportion of the strain is accommodated by stacking fault shear, and the flow stress decreases as a result. The threshold stress to propagate a stacking fault through the precipitate is lower than the yield stress (930 MPa) for the stress strain curves in Figure 1.[10] As strain within the sample increases, more dislocations will shear by the formation of stacking fault ribbons as opposed to APB shearing and the flow stress will drop.

In the tensile test conducted at the strain rate $10^{-6}\ s^{-1}$, the flow stress drops down to around 720 MPa (see the blue curve in Figure 1). This is roughly equivalent to the stress at which primary creep by a stacking fault mechanism in CMSX-4 would produce strain rates of up to $4.4 \times 10^{-6}\ s^{-1}$ during primary creep at 750 MPa and $6 \times 10^{-7}\ s^{-1}$ at 650 MPa, both at and 750 ºC.[10] Using the power law relationship between strain rate and stress plotted in Figure 7 of Reference [10], we can estimate that a creep stress of 665 MPa would be needed to maintain a primary creep strain rate of $10^{-6}\ s^{-1}$. This is slightly lower than the measured flow stress minimum in the slow tensile test of 720 MPa. It assumes a microstructure with a relatively low strain, primary creep ending at about 3 pct strain in CMSX-4 at 750 MPa and 750 °C, whereas the tensile stress minimum corresponds to about 10 pct strain. However, the micrograph from this condition, Figure 1(e), shows that even at this high strain, there is still some undeformed microstructure between the slip bands. Beyond this point in the tensile test, the stress begins to rise again as these dislocations begin to interact and hardening increases the flow stress until failure at 23 pct strain. It is expected that the gradual increase of dislocation debris, particularly in the γ phase, restricts the movement of the dislocation ribbons to a single γ' precipitate, thus reducing their effective velocity. The same occurs in creep where the gradual accumulation of dislocations, particularly in the γ channels, reduces secondary creep rate by a factor of 50 to 100 relative to that of primary creep.[10]

Although the dislocations structure of the a $\langle 121 \rangle$ ribbons is the same in both creep and tensile deformation, the configuration of the ribbon is noticeably different in the interrupted tensile tests reported here in Figure 5. The leading SISF stacking fault is highly constricted across the ribbon with the trailing SESF extended in most cases to the γ/γ' interface. In contrast, in interrupted creep tests, the leading SISF is often extended in the γ' phase and sometimes becomes separated from the trailing SESF by the γ channels (see for example Figure 1 of Ref [10]). Where the ribbon in Figure 5 passes through the γ channel, the APB section in the middle section widens as there is no APB in the disordered γ. This can be clearly seen in the center of the images, particularly Figures 5(a) and (g). In the center of Figure 5(f), small faulted tertiary γ' precipitates can be seen in this central area. During tensile deformation, the strain rate is imposed so the dislocation ribbon will be moving as fast as diffusion will allow. It is likely therefore, that the constricted SISF is the most efficient way of moving this dislocation ribbon. The advantage of a constricted SISF is that it minimizes the segregants necessary to stabilize the fault.

Both leading SISFs and trailing SESFs are segregated by Co and Cr. Barba et al.[31] have measured the levels of segregation in both faults in the single crystal alloy MD2 by integrating measured levels over several planes. They found that for Co, and particularly for Cr, the SISF has higher segregation levels than the SESF. Using their values, we calculate the ratio (SISF/SESF) of excess solute as 1.03 pct/0.62 pct for Cr and 0.48 pct/0.44 pct for Co. Thus for Cr, the SISF requires 66 pct more segregant that the SESF. Under condition where stacking fault ribbons are competing with APB shear operating at a higher stress, it may well be that the leading SISF of the ribbon moves at a lower solute segregation level, albeit at a slightly higher stress. By adopting a lower segregation level, and hence a higher SISF energy and a more constricted fault, the total amount of solute needed would be lower. It is argued that the diffusion of the elements Co and Cr to reduce the stacking fault energy determines the rate at which the dislocation ribbon can move in creep.[31] Hence a more constricted fault, similarly constrained by diffusion, would be able to move faster in a strain rate determined regime such as slow tensile deformation. The single line scan of the SISF in CMSX-4 taken from our tensile tests, Figure 8, suggests an increase in local measured Co and Cr content of about 2 at. pct. This is rather larger than numbers in the alloy MD2 for both elements which have roughly the same concentrations in CMSX-4 and MD2, but the methodology of the measurements is somewhat different.

The observation of the shape adopted by the ribbons suggests that the trailing edge remains in contact with the γ channel as the leading edge progresses and then fairly rapidly breaks away from the γ/γ' interface as no examples showing the trailing partial in transit across the γ' precipitate were seen. A further shuffle is required for the trailing superlattice partial to move through the γ' removing the SESF. By remaining in contact with the γ channel, the supply of Cr and Co to the expanding

SESF may be facilitated as Cr and Co preferentially partition to the γ phase.[33–36] Other sources of excess Cr and Co could include nano-precipitates of γ in the γ'.

C. *Comparison with Other Alloys*

The alloys TMS 138A and SRR99 do not show the dip in flow stress at the slowest strain rate measured, although some evidence of stacking fault shear was observed in TMS 138A. Clearly, the density of dislocations and/or the speed at which they could move does not provide sufficient strain to allow this mechanism to dominate the deformation process. The flow stress remains high in both cases to maintain sufficient APB shear to achieve the imposed strain rate. In the case of TMS 138 A, this is explained by the slower diffusion in the γ phase in this alloy associated with the higher Re content. For example, creep performed on the alloy at 800 °C and 735 MPa resulted in a maximum primary creep rate of around 10^{-8} s^{-1} as measured off the graph presented by Yeh *et al.*[14] This is too slow for SF shear to provide the strain rate of 10^{-6} s^{-1} at the lower temperature of 750 °C. The case of SRR 99 is less clear. The sample was not examined in the TEM so we do not know whether SF shear was occurring but it is certainly a mechanism of creep at similar temperatures in SRR99 and the diffusion in this 1st generation alloy should be lower than in the other two alloys. It has the lowest content of Co (5 wt pct), the, but the Cr levels are the highest. A potential factor may be the W levels in this alloy which are the highest of all three alloys by some margin at 9.5 wt pct. Unlike Re and Mo, which largely replace W in the higher generation alloys and partition strongly to the γ phase, W is equally distributed between the two phases and may have a considerable effect on diffusion in the γ' phase of this alloy. However, it remains unclear why SRR99 does not show a stress dip.

V. CONCLUSIONS

Changing the strain rate had no effect on the yield stress at 750 °C for CMSX-4, with tensile tests at all three strain rates showing similar values of yield stress. However, it does seem to have an effect on post-yield behavior, where at a sufficiently slow strain rate (10^{-6} s^{-1}), a transition in deformation mechanism from APB shearing to stacking fault shearing was observed. This transition was accompanied by a drop in the flow stress, to values typical of primary creep. This transition was not observed in two other alloys tested: TMS-138A and SRR99. Stacking fault shear was demonstrated to occur following the activation of a secondary slip system, allowing dislocations on two different slip systems to interact and enter the precipitate as a SF at a lower stress. This lowered the flow stress as a sufficient density of dislocations propagating by stacking fault shear becomes available. EDX and EELS maps of these stacking faults showed segregation of chromium and cobalt at the stacking faults. This suggests alloy composition plays an important role in causing this transition.

DATA AVAILABILITY

The data used to present these findings can be supplied upon application to the corresponding author.

CONFLICT OF INTEREST

On behalf of all authors, the corresponding author states that there is no conflict of interest.

OPEN ACCESS

REFERENCES

1. D.M. Dimiduk: *J. Phys. III*, 1991, vol. 1(6), pp. 1025–53.
2. B. Kear and H. Wilsdorf: *Trans. Am. Soc. Met.*, 1962, vol. 224, pp. 382–6.
3. D. Caillard: *Mater. Sci. Eng. A*, 2001, vol. 319, pp. 74–83.
4. M. Feller-Kniepmeier, T. Link, I. Poschmann, G. Scheunemann-Frerker, and C. Schulze: *Acta Mater.*, 1996, vol. 44(6), pp. 2397–407.
5. A. Sengupta, S. Putatunda, L. Bartosiewicz, J. Hangas, P. Nailos, M. Peputapeck, and F. Alberts: *J. Mater. Eng. Perform.*, 1994, vol. 3(5), pp. 664–72.
6. M. McLean: *Phil. Trans. Roy. Soc. Lond. A*, 1995, vol. 351, pp. 419–33.
7. Z. Zhu, H. Basoalto, N. Warnken, and R.C. Reed: *Acta Mater.*, 2012, vol. 60, pp. 4888–900. https://doi.org/10.1016/j.actamat.2012.05.0232.
8. L. Kovarik, R.R. Unocic, J. Li, P. Sarosi, and C. Shen: *Progress Mater. Sci.*, 2009, vol. 54, pp. 839–73. https://doi.org/10.1016/j.pmatsci.2009.03.010.
9. B.H. Kear and J.M. Oblak: *Met. Trans.*, 1970, vol. 1, pp. 2477–86. https://doi.org/10.1007/BF03038373.

10. C.M.F. Rae and R.C. Reed: *Acta Mater.*, 2007, vol. 55, pp. 1067–81.
11. C. Cui, Y. Gu, Y. Yuan, and H. Harada: *Scripta Mater.*, 2011, vol. 64, pp. 502–5.
12. T.M. Smith, B.D. Esser, N. Antolin, A. Carlsson, R.E.A. Williams, A. Wessman, T. Hanlon, H.L. Fraser, W. Windl, D.W. McComb, and M.J. Mills: *Nat. Commun.*, 2016, vol. 7, p. 3434. https://doi.org/10.1038/ncomms13434.
13. T.M. Smith, R.R. Unocic, H. Deutchman, and M.J. Mills: *Mater. High Temp.*, 2016, vol. 33, pp. 372–83. https://doi.org/10.1080/09603409.2016.1180858.
14. A.C. Yeh, K. Kawagishi, H. Harada, T. Yokokawa, Y. Koizumi, T. Kobayashi, D. Ping, J. Fujioka, and T. Suzuki, in *Proceedings of the International Symposium on Superalloys*, 2008, pp. 619–28.
15. J. Li, Central symmetry parameter. http://mt.seas.upenn.edu/Archive/Graphics/A/Doc/CentralSymmetry.pdf. Part of AtomEye online manual (August 2003).
16. A.T. Jones and C. Baxter: *Measur. Sci. Technol.*, 1995, vol. 6, pp. 131–33. https://doi.org/10.1088/0957-0233/6/1/021.
17. F. Smith: *Industrial Applications of X-ray Diffraction*, CRC Press, Boca Raton, 1999.
18. D. Crudden, A. Mottura, N. Warnken, B. Raeisinia, and R. Reed: *Acta Mater.*, 2014, vol. 75, pp. 356–70. https://doi.org/10.1016/j.actamat.2014.04.075.
19. T. Pollock and A. Argon: *Acta Metall. Mater.*, 1992, vol. 40, pp. 1–30.
20. H.-J. Chang, M.C. Fivel, and J.-L. Strudel: *Int. J. Plast*, 2018, vol. 108, pp. 21–39. https://doi.org/10.1016/j.ijplas.2018.04.009.
21. G. Scheunemann-Frerker, H. Gabrisch, and M. Feller-Kniepmeier: *Phil. Mag. A*, 1992, vol. 65, pp. 1353–68. https://doi.org/10.1080/01418619208205609.
22. M. Feller-Kniepmeier and G. Scheunemann-Frerker: *Phil. Mag. A*, 1990, vol. 62, pp. 77–88. https://doi.org/10.1080/01418619008244336.
23. V.A. Vorontsov, L. Kovarik, M.J. Mills, and C.M.F. Rae: *Acta Mater.*, 2012, vol. 60, pp. 4866–78. https://doi.org/10.1016/j.actamat.2012.05.014.
24. V.A. Vorontsov, C. Shen, Y. Wang, D. Dye, and C.M.F. Rae: *Acta Mater.*, 2010, vol. 58, pp. 4110–19. https://doi.org/10.1016/j.actamat.2010.03.041.
25. B.H. Kear, A.F. Giamei, G.R. Leverant, and J.M. Oblak: *Scr. Metall.*, 1969, vol. 3, pp. 123–29. https://doi.org/10.1016/0036-9748(69)90214-2.
26. B.H. Kear, A.F. Giamei, G.R. Leverant, and J.M. Oblak: *Scr. Metall.*, 1969, vol. 3, pp. 455–60. https://doi.org/10.1016/0036-9748(69)90130-6.
27. G.R. Leverant and B.H. Kear: *Metall. Mater. Trans. B.*, 1970, vol. 1B, pp. 491–98. https://doi.org/10.1007/BF02811560.
28. L. Kovarik, R. Unocic, J. Li, and M.J. Mills: *JOM*, 2009, vol. 61, pp. 42–48. https://doi.org/10.1007/s11837-009-0026-6.
29. N. Eurich and P. Bristowe: *Scripta Mater.*, 2015, vol. 102, pp. 87–90. https://doi.org/10.1016/j.scriptamat.2015.02.020.
30. G. Viswanathan, R. Shi, A. Genc, V.A. Vorontsov, L. Kovarik, C.M.F. Rae, and M.J. Mills: *Scripta Mater.*, 2015, vol. 94, pp. 5–8. https://doi.org/10.1016/j.scriptamat.2014.06.032.
31. D. Barba, T.M. Smith, J. Miao, M.J. Mills, and R.C. Reed: *Metall. Mater. Trans. A.*, 2018, vol. 49A, pp. 4173–85. https://doi.org/10.1007/s11661-018-4567-6.
32. C.M.F. Rae, N. Matan, and R.C. Reed: *Mater. Sci. Eng. A*, 2001, vol. 300, pp. 125–34. https://doi.org/10.1016/S0921-5093(00)01788-3.
33. R.N. Jarrett and J.K. Tien: *Metall. Trans. A*, 1982, vol. 13, pp. 1021–32. https://doi.org/10.1007/BF02643399.
34. J.K. Tien and R.N. Jarrett, in *Proceedings of a Conference Held in Liège*, Belgium 4–6 October 1982, pp. 423–46. Springer. ISBN-10: 9027714681.
35. A.A. Oni, S.R. Broderick, K. Rajan, and J.M. LeBeau: *Intermetallics*, 2016, vol. 73, pp. 72–78. https://doi.org/10.1016/j.intermet.2016.03.006.
36. S.C.H. Llewelyn, K.A. Christofidou, V.J. Araullo-Peters, N.G. Jones, M.C. Hardy, E.A. Marquis, and H.J. Stone: *Acta Mater.*, 2017, vol. 131, pp. 296–304. https://doi.org/10.1016/j.actamat.2017.03.067.